# Influence of different ester side groups in polymers on the vapor phase infiltration with trimethyl aluminum

Mai, Lukas; Maniar, Dina; Zysk, Frederik; Schöbel, Judith; Kühne, Thomas D.; Loos, Katja; Devi, Anjana

*Published in:*
Dalton Transactions

*DOI:*
10.1039/D1DT03753F

Dalton Transactions

ROYAL SOCIETY OF CHEMISTRY

PAPER

View Article Online
View Journal | View Issue





Cite this: *Dalton Trans.*, 2022, **51**, 1384

# Influence of different ester side groups in polymers on the vapor phase infiltration with trimethyl aluminum†

Lukas Mai, [a] Dina Maniar, [b] Frederik Zysk,[c] Judith Schöbel,[b] Thomas D. Kühne,[c] Katja Loos [b] and Anjana Devi *[a]

The vapor phase infiltration (VPI) process of trimethyl aluminum (TMA) into poly(4-acetoxystyrene) (POAcSt), poly(nonyl methacrylate) (PNMA) and poly(*tert*-butyl methacrylate) (PtBMA) is reported. Depth-profiling X-ray photoelectron spectroscopy (XPS) measurements are used for the first time for VPI based hybrid materials to determine the aluminum content over the polymer film thickness. An understanding of the reaction mechanism on the interaction of TMA infiltrating into the different polymers was obtained through infrared (IR) spectroscopy supported by density functional theory (DFT) studies. It is shown that the loading with aluminum is highly dependent on the respective ester side group of the used polymer, which is observed to be the reactive site for TMA during the infiltration. IR spectroscopy hints that the infiltration is incomplete for POAcSt and PNMA, as indicated by the characteristic vibration bands of the aluminum coordination to the carbonyl groups within the polymers. In this context, two different reaction pathways are discussed. One deals with the formation of an acetal, the other is characterized by the release of a leaving group. Both were found to be in direct concurrence dependent on the polymer side group as revealed by DFT calculations of the IR spectra, as well as the reaction energies of two possible reaction paths. From this study, one can infer that the degree of infiltration in a VPI process strongly depends on the polymer side groups, which facilitates the choice of the polymer for targeted applications.

Received 6th November 2021,
Accepted 17th December 2021

DOI: 10.1039/d1dt03753f

rsc.li/dalton

## Introduction

In times of an enormous demand on highly efficient computer chips, flexible electronics and other nanotechnology products, the interest in inorganic–organic hybrid materials is rapidly increasing. This derives from the advantageous fusion of properties of inorganic materials with those of organic materials. For example, a high mechanical resistance as found in ceramics or tunable electrical conductivity, known from semiconductors or metals may be combined with the flexibility and light weight of an organic polymer.[1–5]

Typically, different thin film architectures or nanolaminates are used for the functionalization of surfaces in nanotechnology devices. Hence, atomic layer deposition (ALD),[6,7] is combined with molecular layer deposition (MLD),[8] for the fabrication of hybrid materials. In this atomic/molecular layer deposition (ALD/MLD) technique,[1,5,8] an inorganic precursor, commonly a metalorganic complex, is brought to reaction with a substrate surface and subsequently with an organic precursor, separated by inert gas purges, to form the hybrid material, layer by layer with an atomic level precision. However, since the reactions in ALD/MLD need a certain activation energy, and some organic molecules can only be vaporized at elevated temperatures, the deposition temperature of such processes is often above the glass transition temperature of most polymers,[9,10] which is limiting the use in flexible applications.

Based on the ALD technique, vapor phase infiltration (VPI) was developed in which the inorganic precursor infiltrates an organic polymer substrate, thereby directly transforming it into a hybrid material, without the need of a volatile organic co-reactant.[1,3,11] This approach is known since 2009, when Knez *et al.* reported an increased toughness of spider silk

[a]*Inorganic Materials Chemistry, Ruhr University Bochum, Universitätsstr. 150, 44801 Bochum, Germany. E-mail: anjana.devi@rub.de*
[b]*Macromolecular Chemistry & New Polymeric Materials, Zernike Institute for Advanced Materials, University of Groningen, Nijenborgh 4, 9747 AG Groningen, Netherlands*
[c]*Dynamics of Condensed Matter and Center for Sustainable Systems Design, Chair of Theoretical Chemistry, Paderborn University, Warburger Str. 100, 33098 Paderborn, Germany*

†Electronic supplementary information (ESI) available. See DOI: 10.1039/d1dt03753f

which was achieved by infiltrating it with Al, Zn or Ti precursors.[12] Furthermore, in a recent study it was found that VPI is also contributing to ALD processes when polymeric substrates are used.[13] The VPI mechanism consists of three steps: dissolution of the precursor in the polymer, diffusion of the precursor and by-products through the polymer structure and entrapment of the precursor by reaction with the polymer chains.[11] Thus, from a precursor point of view, apart from the typical ALD criteria volatility, thermal stability and reactivity,[14–16] especially shape, size and polarity of the molecule play a major role for dissolution and diffusion processes and can be tuned for the desired hybrid properties.[17,18] However, as substrate in VPI, the physico-chemical properties of the organic polymer play a crucial role as well, as its free volume and tortuosity majorly contribute to the dissolution and diffusion processes and the functional groups not only determine the reactivity but also may release by-products that need to diffuse off the polymer.[9,19,20] Logically, the infiltration temperature is influencing all three parameters, *i.e.* dissolution, diffusion and reactivity drastically.[21,22]

Varying just one of these parameters, can change the infiltration behavior and the resulting hybrid properties, which opens a versatile playground for different applications. For example, hybrid-polymers from VPI were used as gas barrier layers[23] or in membranes[24] because of a changed diffusivity of gases through the hybrid material as compared to the bare polymer. Additionally, by controlling the amount of metal that is infiltrated into the polymer, the conductivity can be tuned, which for example is used in solar cells.[25,26] Furthermore, many transformed hybrid-polymers are known to have an increased mechanical strength[12,21,27–29] and chemical resistance,[30] which enables, among other applications, a new patterning procedure in lithography processes.[31–33]

Especially for the latter application, the infiltration of poly (methyl methacrylate) (PMMA) and the block copolymer of PMMA and polystyrene (PS) with trimethylaluminum (TMA) was investigated, as PMMA exhibits a large free volume which enables a fast and easy infiltration.[30,34–39] Hence, the VPI process could be of high interest for the semiconductor industry as it can easily be performed in existing ALD equipment. However, to understand which material is formed during the infiltration and how this changes the properties for a desired application, knowledge about the interaction of the precursor with the polymer is needed. Elam *et al.*[38] as well as Parsons and co-workers[39] have postulated a reaction mechanism of TMA with PMMA which results in two different reaction products. While both groups observed an initial coordination complex of TMA to the carbonyl group of the polymer, Elam *et al.* postulated a rearrangement of that complex to form an acetal structure. Parsons *et al.* observed a cleavage of the methylated side group of the ester by reaction of a methyl group of TMA with the ester function. In this context, the aim of this study is to investigate the influence of the side group of the ester function in different polymers, structurally related to PMMA, on the VPI of TMA and to gain insight into the underlying mechanism.

Here, we present the development of a VPI process of TMA into spin-coated poly(4-acetoxystyrene) (POAcSt), poly(nonyl methacrylate) (PNMA) and poly(*tert*-butyl methacrylate) (P*t*BMA) on Si(100) at 85 °C and varied pulse times of TMA. The infiltration is evaluated by depth profiling of the 40 nm thick polymer samples *via* X-ray photoelectron spectroscopy (XPS) in combination with $Ar^+$ sputtering, which is a new approach for VPI processes that directly delivers a depth dependent composition of the thin films. Furthermore, the transformed hybrid polymers are investigated by infrared (IR) spectroscopy accompanied by density-functional-theory (DFT) calculations to determine the more probable reaction products and attain deeper insight into the mechanism and reaction products.

## Results and discussion

The solutions of the three targeted polymers (i) POAcSt, (ii) PNMA and (iii) P*t*BMA were synthesized and spin coated on Si(100) substrates. The thickness was determined by ellipsometry. Subsequently, they were loaded on a heated substrate holder (85 °C) in an ALD reactor under a vacuum ($10^{-5}$ mbar). In the next step, the infiltration process was performed, the details of which are provided in the Experimental section. For the VPI process, the precursor must dissolve in the polymer, diffuse through it and finally react with the functional groups of the polymer.[11] Afterwards, the reaction products must be able to leave the polymer. Therefore, the reactor was used in a static vacuum condition (*i.e.*, the valve between pump and reaction chamber was closed after the base pressure was reached) during the precursor pulse to ensure a sufficient TMA pressure around the substrate during the soaking time. Furthermore, in a static vacuum a high concentration gradient is generated which accelerates the diffusion processes. Finally, after the precursor pulse and a vacuum purge, one water pulse was used to fix all unreacted Al–$CH_3$ groups as Al–OH within the sample.

The XPS depth profiles of all infiltrated polymers are depicted in the ESI (Fig. S1†). The contents of the elements Al (red squares), C (blue circles), O (green triangles) and Si (black stars) are given in dependence of the etching time into the polymer which is directly correlated to the depth. As evident, the time to etch through an approximately 40 nm thick infiltrated polymer layer is strongly dependent on the polymer material. Here, PNMA is etched already after ~200 s, P*t*BMA after ~250 s and POAcSt after ~550 s which is indicated by an increased Si signal from the underlying substrate. Thus, the supposed small changes in the molecular structure of the polymers, as depicted in Fig. 2, have a huge influence on the polymer properties already.

The infiltration of TMA into the polymers can be tracked by the aluminum content which is depicted in Fig. 1 for the different polymers and TMA pulse times. As depicted, the successful VPI of aluminum into the three polymers investigated in this study with TMA can be confirmed. The completeness of

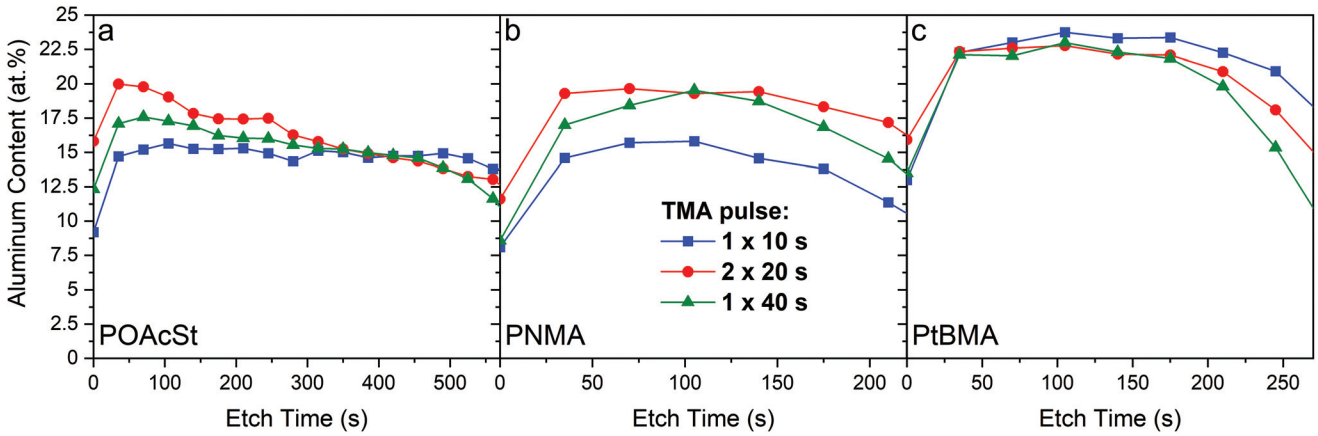


**Fig. 1** Aluminum content of the polymers POAcSt (a), PNMA (b) and PtBMA (c) after VPI with TMA doses of 1 × 10 s (blue squares), 2 × 20 s (red circles) and 1 × 40 s (green triangles).

the infiltration process is indicated by a nearly constant aluminum content over the whole 40 nm thick polymer layer.

In case of POAcSt (Fig. 1a), the aluminum content saturates with a concentration of around 15 at.%, which is already reached for the shortest TMA pulse time of one 10 s pulse. Interestingly, with a 40 s pulse, the aluminum seems to accumulate at the surface. This trend is even stronger for two 20 s pulses of TMA in between of which vacuum was applied and could be attributed to the different reactions that TMA can undergo with POAcSt as depicted in Fig. 2a.

Elam *et al.*[38] as well as Parsons and co-workers[39] postulated two different reaction mechanisms that ester groups can undergo with TMA during VPI (R1 and R2 in Fig. 2). Both mechanisms are starting with an intermediate adduct of TMA with the carbonyl function of the ester. The first one is an addition of one methyl group of TMA to the carbon atom of the ester function to form an acetal in which one oxygen is bonded to dimethylaluminum (R1 in Fig. 2). In case of POAcSt, the second mechanism would result in cleavage of dimethylaluminum acetate from the polymeric chain (R2 in Fig. 2), which is a relatively small and volatile compound. Thus, for the longer TMA pulse time, an increased diffusion of dimethylaluminum acetate along the concentration gradient, *i.e.*, toward the surface might result in an accumulation of aluminum near the surface. This is supported by the fact, that this effect is stronger for the 2 × 20 s pulses when a turbopump vacuum is applied in between the pulses which elongates the total time of the sample in vacuum and increases the speed of diffusion. Another explanation could be that once all reactive sites of the polymer chains have taken part in the reaction with TMA, the infiltrated polymer has different properties and diffusion of TMA into the hybrid-polymer is hindered. This will also result in an accumulation of aluminum near the surface which is trapped in the polymer by a reaction with unreacted polymer chains or with water in the last step.

For PNMA the situation is different as illustrated in Fig. 1b. For the longer exposure times of one 40 s pulse or two 20 s pulses, the aluminum content is saturating at around ~20 at.%, while two times 20 s seem to result in a more homogeneous distribution of the aluminum over the polymer depth profile. Furthermore, for the shortest one time 10 s pulse, the infiltration is not complete with an aluminum concentration of ~15 at.%. These results seem to be surprising considering the glass transition temperature ($T_g$, *cf.* Fig. S2†) of PNMA. While POAcSt and P*t*BMA show $T_g$'s of 123 °C and 117 °C, respectively, which is well above the applied infiltration temperature of 85 °C, PNMA exhibits a considerably lower $T_g$ of −28 °C. Since the glass transition temperature of polymers is defined as the temperature, above which the chain segment mobility of the amorphous chains is enabled, the amorphous PNMA chains are expected to be mobile at the given infiltration temperature. The chain mobility should lead to an enhanced infiltration process of TMA through the polymer chains. However, the contrary behavior is observed, which can be explained by the structure of the polymer as outlined in Fig. 2b. In PNMA, a long nonyl-group is attached to the ester function, which significantly increases the diffusion paths of TMA toward reaction sites. Thus, the tortuosity is increased for PNMA. Furthermore, considering the two reaction mechanisms, the reaction product of PNMA and TMA will result either in an even more bulky acetal or releases an *n*-decane ($C_{10}H_{22}$) molecule that is hindered in diffusion from the polymer due to its large size and the high boiling point (174 °C at 1 atm). This might explain the more homogenous distribution of aluminum for the two 20 s TMA pulses, as the additional vacuum step leads to a decrease in the boiling point and therefore enhances the diffusion of the large $C_{10}H_{22}$ molecules through the polymer.

The highest amount of aluminum with a homogeneous distribution for the whole polymer depth can be found for P*t*BMA as depicted in Fig. 1c. Here, all TMA pulse times, including the shortest 10 s pulse, result in a high aluminum concentration of ~23 at.%. This finding is explainable by the size of a P*t*BMA unit which is the smallest of all polymers (*cf.* Fig. 2c). Combined with the small but bulky *tert*-butyl ($^t$Bu) group at the ester function, this increases the free volume of the polymer, which enhances the diffusion. Furthermore, the reac-

 

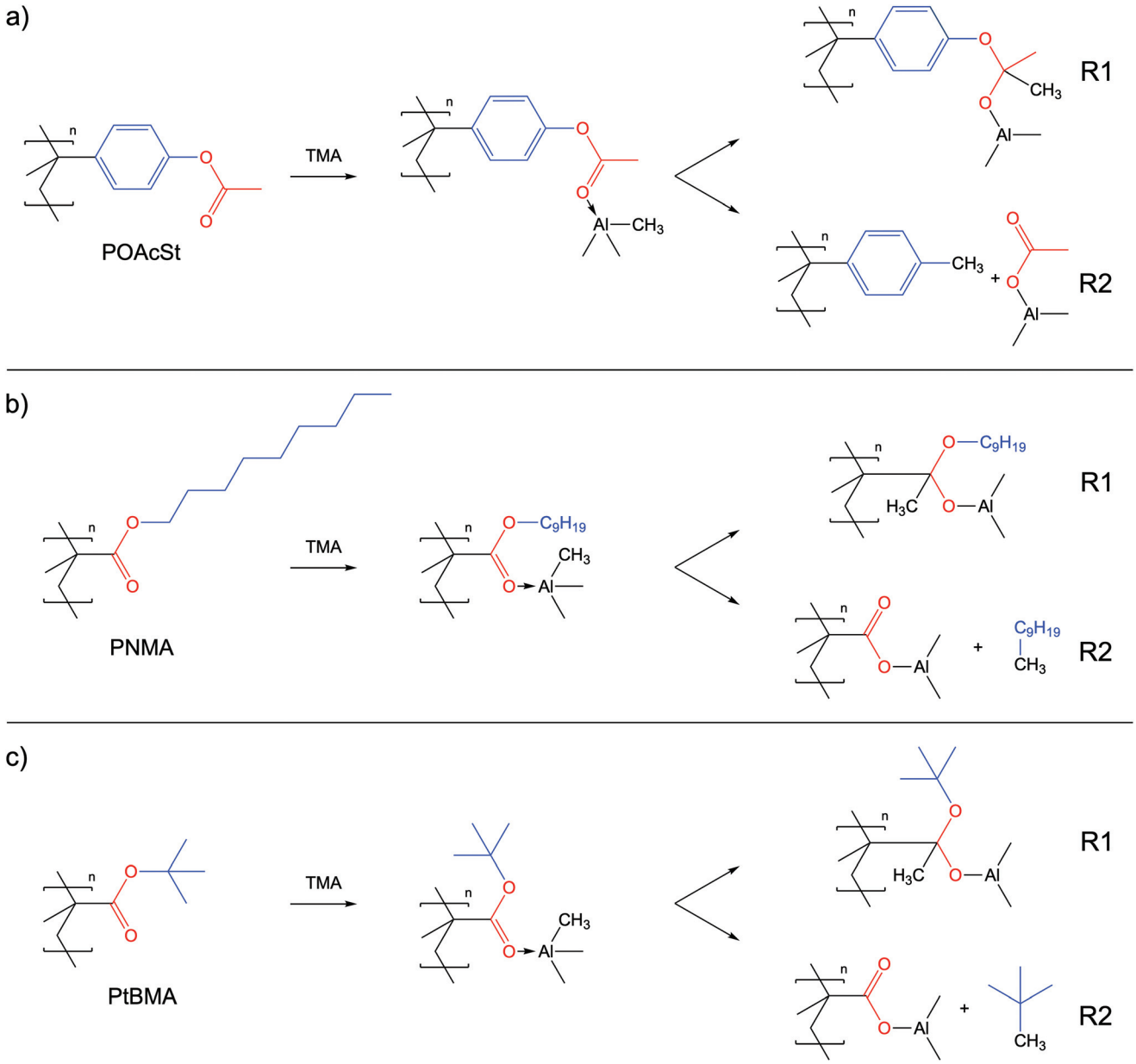


**Fig. 2** Chemical structure of the polymers poly(4-acetoxystyrene) (POAcSt) (a), poly(nonyl methacrylate) (PNMA) (b) and poly(*tert*-butyl methacrylate) (P*t*BMA) (c), and possible reactions that the polymers can undergo during the VPI experiments according to Elam *et al.*[38] (R1) and Parsons *et al.*[39] (R2).

tion with TMA might release a neopentane ($H_3C$-$^t$Bu) molecule which is gaseous at process conditions and therefore more likely to diffuse from the polymer as compared to the *n*-decane of the previously described PNMA. Thus, the diffusion rate is the highest for P*t*BMA which results in a complete reaction of TMA even for very short pulses.

For both polymethacrylates (PNMA and P*t*BMA) no accumulation of aluminum near the surface could be observed. In POAcSt, however, the aluminum is part of a potential leaving group and cannot be attached to the polymeric chain anymore. As this accumulation is not the case for the other two polymers, it is indicating that the leaving group plays a major role in the reaction of TMA with polymers.

Interestingly, the detected amount of Al in all polymers seems to be higher than theoretically expected from the reactions R1 or R2. For example, in POAcSt the ratio between carbon and aluminum, as evident from Fig. S1,† should be C/Al = 12 in case of R1 and R2 if the leaving group remains within the polymer. However, the detected values range between C/Al ~ 3–4. For PNMA, C/Al ratios between 14 and 4 should be expected depending on the reaction path R1 or R2, respectively, but values between 2.5 and 3.5 are detected.

Lastly, in P*t*BMA the C/Al ratios should be within 9 and 4, for R1 and R2, but values around 2 were measured. This indicates that either during sputtering in the XPS experiment the carbon is preferentially removed, or a second reaction of TMA with the polymer chain takes place which might be indicated by investigations of reactions of TMA with ester containing lubricants in toluene solution.[57,58] A third option would be that the time for excess TMA within the polymer was too short to diffuse off the polymer before it was trapped by reaction with water to form aluminum oxide during the water pulse. Of course, all three phenomena may occur at the same time.

To gain further insights into the infiltration process, Fourier-Transform Infrared (FT-IR) spectroscopy was performed of the untreated polymers as well as the polymers after infiltration with TMA employing two 20 s pulses. For a comparison, the spectra are merged in Fig. 3 and the prominent IR modes have been assigned to their respective vibrations within the molecular structure based on the IR modes identified by Parsons and co-workers.[39] Prior to the infiltration, typical IR modes of the polymers are arising such as the C–H stretch vibrations between wavenumbers of 2800 $cm^{-1}$ and 3000 $cm^{-1}$ for all three polymers as well as the aromatic C=C vibration at 1506 $cm^{-1}$ in case of POAcSt.[40] Furthermore, the carbonyl vibration at 1763 $cm^{-1}$, 1728 $cm^{-1}$ and 1718 $cm^{-1}$ for POAcSt, PNMA and P*t*BMA respectively is a prominent vibration mode in all three spectra. Additionally, the O–C vibration of the ester side group can be found at 1023 $cm^{-1}$ and 1128 $cm^{-1}$ for PNMA and P*t*BMA, respectively,[37,41] while for POAcSt this specific IR mode is not arising but the characteristic acetyl C–O vibration at 1223 $cm^{-1}$ is visible.[40]

After infiltration with TMA and subsequent reaction with water, distinct differences in the spectra as compared to the bare polymers can be observed. First, an IR mode between 3500 $cm^{-1}$ and 3750 $cm^{-1}$ assignable to O–H vibrations can be found in every infiltrated sample.[40] This could explained by water that did not diffuse off the polymer after the infiltration which becomes possible due to a more polar hybrid polymer due to the introduction of aluminum into the polymer films. Furthermore, after the reaction of TMA with the polymer chains, the aluminum alkyl compounds will still react with water or air to form aluminum hydroxide species within the films that also can contribute to the O–H vibrations.

In addition to the XPS results, indicating a significant amount of Al in the films, the existence of aluminum within the films is further proven by the Al–O vibration mode at 882 $cm^{-1}$, 878 $cm^{-1}$ and 880 $cm^{-1}$ in POAcSt, PNMA and P*t*BMA, respectively, after the infiltration process.[38,42] Interestingly, a sharp peak arises around 700 $cm^{-1}$ in all polymers after TMA infiltration which might be an indication of remaining, unreacted Al–C bonds.[37,43]

Further changes in the IR spectra after the VPI with TMA can be observed in the O–C vibration of the ester side groups, which are disappearing or at least diminishing after infiltration for PNMA and P*t*BMA. In the case of POAcSt, the vibration of the acetyl C–O group is slightly decreased in intensity. This might be ascribed to a predominant reaction path R2 (Fig. 2)

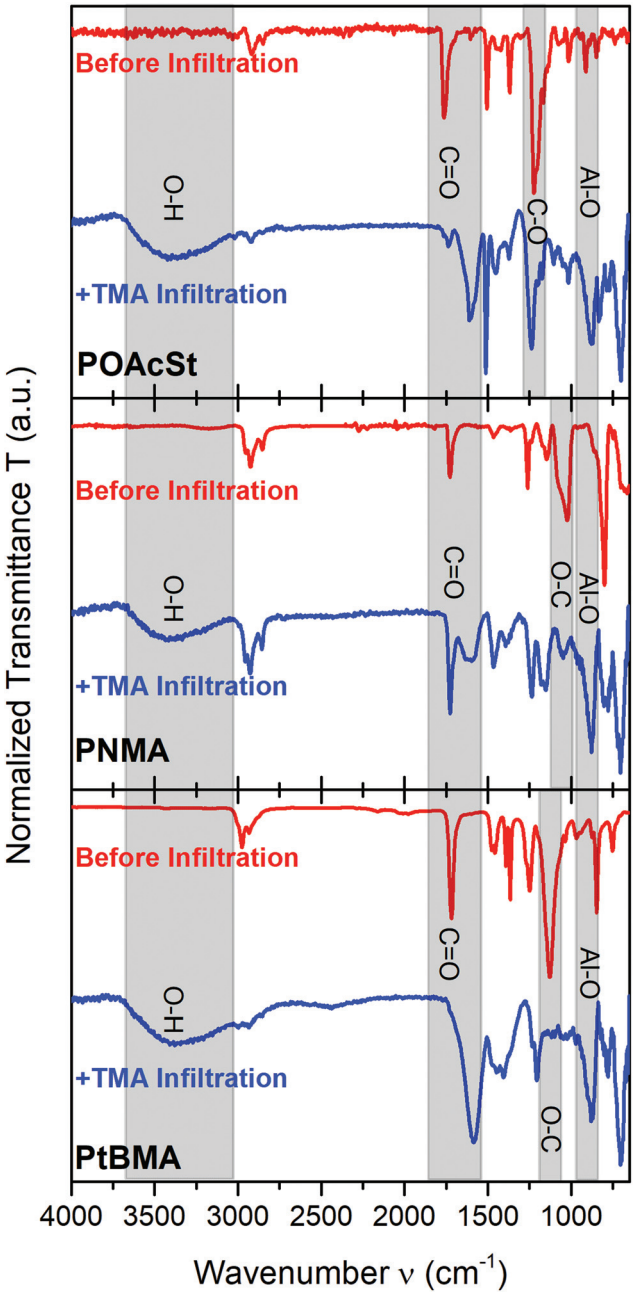


**Fig. 3** FT-IR spectra with assigned IR modes of POAcSt (top), PNMA (middle) and P*t*BMA (bottom) before (red) and after infiltration (blue) with TMA using two 20 s pulses.

where the O–C bond is exchanged by an O–Al bond in PNMA and P*t*BMA, while for POAcSt the acetyl group is completely transferred to the leaving group and thus, might partly diffuse off the polymer.

The last significant change in the IR spectra can be observed within the C=O vibration. Here, a shift can be observed that was described by Parsons *et al.*[39] as a reason of a bridging Al center to two different carboxylic groups after reaction path R2 (Fig. 2). In POAcSt, the peak is shifted to 1611 $cm^{-1}$ while a small contribution is not shifted, indicating

some unreacted ester groups, which is similar for PNMA where the C═O vibration caused a broader peak with a center at 1611 $cm^{-1}$. In PNMA the unreacted ester groups show the most intense signals as compared to the other polymers, indicating that the large side groups are drastically hindering diffusion of TMA and reaction products within the polymer due to the high tortuosity. Probably, with longer pulsing and purge times a higher amount of aluminum can be achieved in PNMA. A complete hybrid transformation can be observed for P*t*BMA where the initial peak completely disappears and is shifted to 1589 $cm^{-1}$. This finding is also in line with the XPS results which show the highest amount of aluminum in the P*t*BMA films for the investigated polymers. In general, especially the C═O vibration is indicating that reaction path R2 from Fig. 2 is the dominant, as a formation of an acetal would result in a diminished or disappeared signal for that IR mode.

Apart from the experimental IR analysis, computational IR calculations were performed to analyze which reaction pathway is more likely to occur. For that, the IR spectrum of the bare polymer POAcSt, PNMA and P*t*BMA was calculated and subtracted from the calculated IR spectrum from one repeating unit of the polymer chain according to path R1 or R2. That means in case of R2, the leaving group was assumed to completely be diffused off the polymer and was not part of the calculation anymore. The resulting relative IR spectra are shown in Fig. 4 and compared to the relative experimental spectra (calculated from the data depicted in Fig. 3 in a range from 700 $cm^{-1}$ to 2000 $cm^{-1}$).

A positive value of the relative IR spectrum (greater than the gray dotted zero-line) means, the corresponding IR peak at that wavenumber increases after infiltration, while a negative deviation would mean a diminishing intensity. This is true for both, the theoretical and experimental spectra in Fig. 4. Absolute values should not be compared, as for these calculations several simplifications, such as the calculation of repeating units instead of polymers and the neglection of diffusion and steric phenomena were made. Therefore, theoretical calculations commonly show a variance in wavenumbers of normal modes which is often combated with frequency scale factors depending on the system and used exchange–correlation functional.[44] Here, no correction factor was used and thus, only the qualitative trend can be compared.

First, in all polymers the described shift of the C═O bond due to a bridging Al center between two carboxylic acid groups, as reported by Parsons *et al.*,[39] is not observed in the simulation since this effect is not possible due to the location of the functional groups in our theoretical model.

For the theoretical and experimental relative IR spectra of POAcSt, it is striking that the experimental trend is following well that of the theoretical curve of R1 in the range from 1000 $cm^{-1}$ to 1500 $cm^{-1}$. Especially between 1100 $cm^{-1}$ and 1300 $cm^{-1}$ (marked in blue) it is matching well with the spectrum of the reaction products of pathway R1 showing a positive experimental deviation at ~1250 $cm^{-1}$, negative at ~1200 $cm^{-1}$ and positive again at ~1100 $cm^{-1}$. The frequency range from

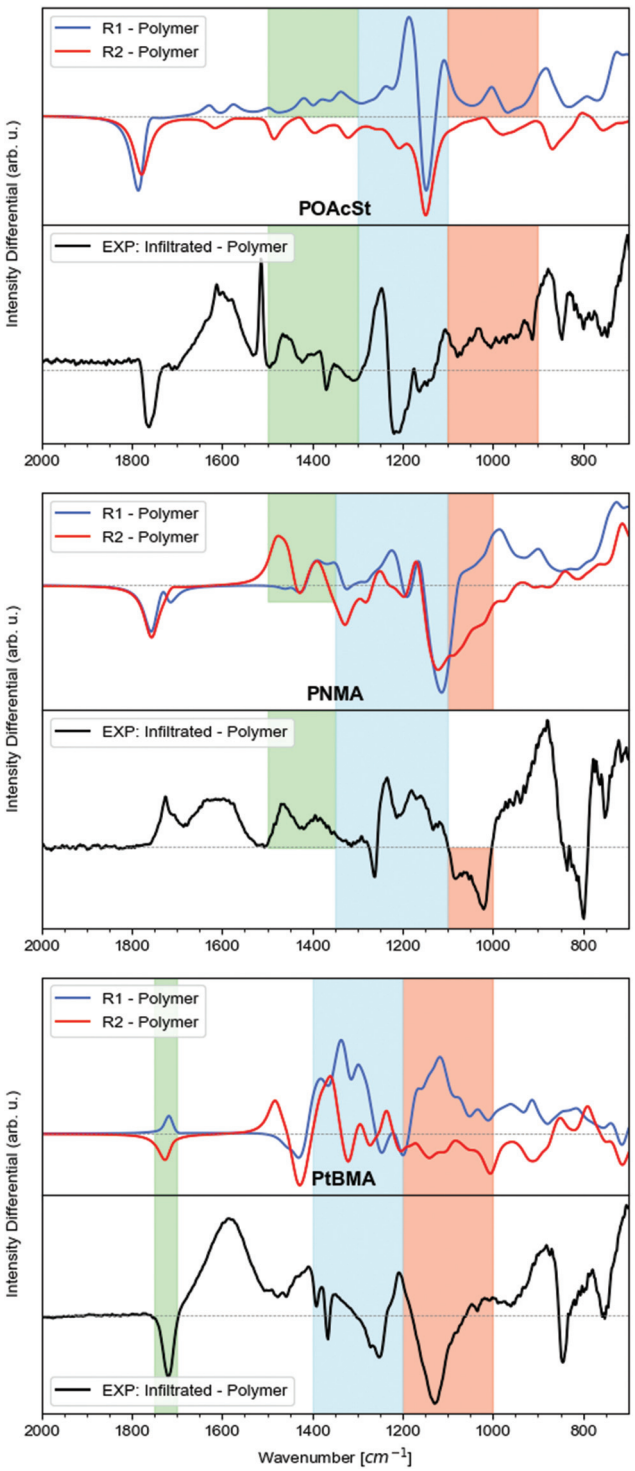


**Fig. 4** Difference of the calculated IR spectra of one monomer of the polymeric chain of pathway R1 (blue) or R2 (red) and the pure polymer POAcSt (top), PNMA (middle) and P*t*BMA (bottom), respectively. For comparison, the difference of the experimental IR spectrum after infiltration with TMA and the respective bare polymer are shown at the bottom of each panel (black). Note: for pathway R2 the leaving group was not used for the IR calculations as a complete diffusion off the polymer was assumed. The frequency ranges of interest are highlighted in colors.

1100 $cm^{-1}$ to 900 $cm^{-1}$ (highlighted in red) also aligns well with the calculated IR spectrum of the reaction products of pathway R1, showing two positive peaks and a positive absolute differential. Differences for the Al–O vibration at ~880 $cm^{-1}$ between the experimental and theoretical trend could be explained by the fact that in POAcSt for R2 no Al is present after infiltration, as it was assumed to diffuse off the polymer as part of the leaving group. In total, the good match of the trends in the range between 1000 $cm^{-1}$ and 1500 $cm^{-1}$ is indicating that R1 is occurring for POAcSt, which is in agreement with the high amount of around ~15 at% Al found within the infiltrated samples. However, the found gradient toward a higher Al content on the polymer surface is indicating that pathway R2 is also present, which is not considered in the IR calculations due to the complete removal of aluminum acetate. Thus, most likely both reaction pathways are in direct competition, occurring at the same time. Therefore, the leaving group from R2 can still be fixed near the surface due to a second or even third reaction of the Al–$CH_3$ groups and polymer chains during the diffusion of the dimethyl aluminum acetate, maybe also creating some crosslinking.

For PNMA, within the range from 1000 $cm^{-1}$ to 1500 $cm^{-1}$ the qualitative course of the spectra cannot be assigned to just one of the reaction paths. Marked in green, the positive peak at 1400 $cm^{-1}$ and 1450 $cm^{-1}$ is following more the trend of the spectrum from the products of pathway R2. Furthermore, the overall negative deviation between 1000 $cm^{-1}$ and 1100 $cm^{-1}$ (highlighted in red) fits to the spectrum of path R2 to a higher extent and is not aligning with R1 in absolute value or trend. However, in the area marked in blue between 1100 $cm^{-1}$ and 1350 $cm^{-1}$, the course of the relative IR spectra cannot align to any specific peak from the experimental data, indicating that again both reaction pathways are present during the infiltration with TMA even though pathway R2 seem to be more dominant.

For P*t*BMA there are three highlighted areas within the spectrum as well. Even though the peak at around 1725 $cm^{-1}$ (highlighted in green) agrees with the spectrum of the products of pathway R2, the results in that area must be taken with care because of the model used in the calculation as described above. In the frequency range between 1200 $cm^{-1}$ and 1400 $cm^{-1}$ (highlighted in blue), it is not possible to align the experimental differential with the spectra of pathway R2 or R1, considering the inaccuracy of absolute values. Only the distinct peak at 1200 $cm^{-1}$ could indicate dominance of pathway R2. The strongest indication can be found in the area highlighted in red, where the experimental differential shows a strong negative peak at 1125 $cm^{-1}$. As this was already attributed to the O–C vibration of the ester, we would expect this deviation to be negative (diminishing peak intensity) for pathway R2, but positive for path R1, which is in well alignment with our findings. Concluding, this indicates that reaction pathway R2 is probable to be the dominant reaction path for P*t*BMA. However, pathway R1 cannot ruled out completely due to the given simplifications necessary for the theoretical calculations.

To identify which of the illustrated reaction pathways (Fig. 2) is more likely and to strengthen the mentioned hypotheses with respect to the reaction mechanisms, the reaction energies were calculated from geometry optimized structures of one monomer of the polymers before infiltration, TMA and the possible monomeric product of the reactions. The found values are given in Table 1 and pictures of the optimized structures are shown in Fig. S3 in the ESI.† First, all the potential energy differences are negative indicating that all reactions are energetically favored. Second, if only reaction pathway R1 would occur, it is most favorable for PNMA with $E_{R1}$ = −1.418 eV, followed by POAcSt ($E_{R1}$ = −1.170 eV) and P*t*BMA ($E_{R1}$ = −0.656 eV). Furthermore, reaction path R2 is most likely for PNMA with $E_{R2}$ = −2.454 eV in a row with P*t*BMA ($E_{R2}$ = −2.153 eV) and POAcSt ($E_{R2}$ = −1.626 eV). The finding, that for PNMA both reactions are most favorable is in line with the finding of competing reaction from our theoretical IR analysis. Interestingly, from the experimental IR analysis there is evidence that the infiltration with TMA is not complete to the highest extent compared to all investigated polymers, even though the reactions are most favored. However, at this point it needs to be noted that the theoretical calculation is only giving the reaction energy of TMA and one monomer which are already in proximity and thus not including diffusion phenomena and the high tortuosity of PNMA. From the absolute energy values, it is striking that pathway R2 is for all three polymers the more favored one as indicated by more negative energy values. This is in line with the XPS results, as well as the experimental IR analysis and explains the accumulation of Al near the surface of the POAcSt samples which is possible because of an Al containing leaving group. To create an idea to what extent the two reactions occur within the polymers, the energy difference $E_{R2} - E_{R1} = \Delta E_{R21}$ can be used. The largest difference can be found for P*t*BMA with $\Delta E_{R21}$ = −1.497 eV, followed by PNMA with a difference of $\Delta E_{R21}$ = −1.036 eV and POAcSt with $\Delta E_{R21}$ = −0.456 eV. In other words, this finding means that R2 is highly favored for P*t*BMA, while a mixture of both reaction paths is most probable for POAcSt. This could explain the complete and fast transformation of the P*t*BMA samples into its Al-hybrid which is possible due to the fast diffusion of the neo-pentyl leaving group compared to the other polymers. On the other hand, for PNMA diffusion phenomena are playing a more significant role due to a higher tortuosity because of the large side groups. For POAcSt, cross linking may need to be considered due to a reactive leaving group that can diffuse within the polymer, which is further decreasing the diffusion speed due to a reduced free volume of the hybrid as well as a higher tortuosity.

**Table 1** Calculated energies for the reactions following pathways R1 and R2 shown in Fig. 2

| | POAcSt | PNMA | P*t*BMA |
|---|---|---|---|
| $E_{R1}$ (eV) | −1.170 | −1.418 | −0.656 |
| $E_{R2}$ (eV) | −1.626 | −2.454 | −2.153 |
| $E_{R2} - E_{R1}$ (eV) | −0.456 | −1.036 | −1.497 |

While this study is a step to understand the mechanism behind VPI processes, further studies about the application of these infiltrated polymers in photolithography, membranes or gas barriers should be performed.

## Conclusions

New VPI processes of TMA into POAcSt, PNMA and P*t*BMA were successfully developed. The amount of Al was determined by XPS depth profiling, indicating that for smaller side groups at the ester function, the infiltration amount of TMA is increasing from 15 at.% over 20 at.% to 23 at.% for two 20 s TMA pulses in POAcSt, PNMA and P*t*BMA, respectively. This may be explained by the increased tortuosity for larger side groups, which is furthermore confirmed by IR spectroscopy experiments. Here, a shift of the C=O vibration to lower wavenumbers is indicating that only for P*t*BMA the infiltration is completed while for POAcSt and especially in PNMA, with the highest tortuosity, unreacted C=O groups can be detected. Theoretically calculated IR spectra indicate that two different reaction mechanisms are possible which are competing during infiltration. While POAcSt is mainly showing functions of a pathway that results in a crosslinked acetal polymer, in P*t*BMA the cleavage of the ester side group as a leaving group is predominant. However, even for POAcSt, this leaving group is created as an accumulation of Al near the polymer surface that would be in line with an aluminum acetate leaving group. This is also confirmed by the calculated reaction energies which indicate that the cleavage of a leaving group is preferred over the formation of an acetal by a lower reaction enthalpy.

Currently, we are investigating the infiltrated polymers as gas barrier material, where this study helps to understand the mechanism of vapor phase infiltration processes of Al into the polymers to fine tune the materials properties. In future, this approach can also be extended to other polymers of interest and this valuable information can be adopted to produce chemically defined inorganic–organic hybrid materials which should be tested for further applications such as photolithography or membranes.

## Experimental

### Polymer processing

**Materials.** Poly(nonyl methacrylate) (PNMA) ($\overline{M_n} = 17\,500$, $\overline{M_w} = 24\,500$, $Đ = 1.4$) and Poly(*tert*-butyl methacrylate) (P*t*BMA) ($\overline{M_n} = 15\,200$, $\overline{M_w} = 15\,400$, $Đ = 1.0$) were purchased from Polymer Source (Canada). 4-Acetoxystyrene (OAcSt), RAFT agent and AIBN were purchased from Sigma-Aldrich. Absolute methanol (MeOH, AR) was obtained from Biosolve Chemicals. OAcSt was dried with calcium hydride ($CaH_2$) overnight at room temperature under argon and distilled before used.

**Synthesis of poly(4-acetoxystyrene) (POAcSt).** In a dried Schlenk tube, 3 mL OAcSt (19.61 mmol, 62 eq.), 128 mg S-(thiobenzoyl)thioglycolic acid (TBTGA, 0.316 mmol, 1 eq.) and 10.5 mg AIBN (0.0632 mmol, 0.2 eq.) were dissolved until a homogeneous pink solution was observed. Then, the Schlenk tube was placed in a pre-heated oil bath (70 °C) and the mixture was stirred for 15 h. To stop the reaction, the Schlenk tube was placed in liquid nitrogen. The polymer was allowed to attain room temperature and was dissolved in THF. The solution was precipitated twice from a tenfold excess of methanol and dried in a vacuum oven (40 °C, 100 mbar). After final drying, a pink powder was obtained ($\overline{M_n} = 11\,600$, $\overline{M_w} = 15\,600$, $Đ = 1.3$).

**Preparation of polymer solutions and spin coating procedure.** Initially, POAcSt, P*t*BMA, and PNMA polymer solutions were prepared by dissolving 1.5–2 wt.% of POAcSt powder in cyclopentanone, and P*t*BMA and PNMA powder in toluene, respectively. Then the solutions were filtered twice through a syringe filter (0.2 μm PTFE) to avoid dust contamination. Polymer thin films were formed by spin coating an adequate amount of each polymer solution at 3000 to 5000 rpm for 60 s onto Si wafers. Prior to spin coating, the Si wafers were cleaned by a snow jet, treated with UV/$O_3$ for 10 min, and finally cleaned again by the snow jet to remove any adsorbed particles. After spin coating, the polymer-coated Si wafers were dried in a vacuum oven at 40 °C overnight (100 mbar), to remove the residual solvent from the polymer films. Ellipsometry measurements of the polymer films spun onto Si wafers confirmed average film thicknesses of around 40 nm.

**Analytics.** Molecular weights (number-average, $\overline{M_n}$, and weight-average, $\overline{M_w}$) of POAcSt were determined by size exclusion chromatography (SEC) equipped with a triple detector, consisting of a Viscotek Ralls detector, Viscotek Viscometer model H502, and Schambeck RI2912 refractive index detector. The separation was carried out by utilizing two PLgel 5 μm MIXED-C, 300 mm columns from Agilent Technologies at 35 °C. THF 99 + %, extra pure, stabilized with BHT was used as the eluent at a flow rate of 1.0 mL $min^{-1}$. Data acquisition and calculations were performed using Viscotek OmniSec software version 5.0. Molecular weights were determined based on a conventional calibration curve generated from narrow dispersity polystyrene standards (Agilent and Polymer Laboratories, $\overline{M_w} = 645 - 3\,001\,000\ g\ mol^{-1}$). The samples were filtered over a 0.2 μm PTFE filter prior to injection.

The thickness of the polymer thin films was evaluated using a V-VASE variable-angle spectroscopic ellipsometer from J. A. Woollam Co. (Lincoln, NE). The values of $\psi$ and $\Delta$ recorded within a range of wavelength included between 300 and 1700 nm using focusing lenses at 70° to 75° from the surface normal. Fitting of the raw data was performed based on a three-layer model (Si/$SiO_2$/Cauchy) using bulk dielectric functions for Si and $SiO_2$. The copolymer layers were analyzed on the basis of the Cauchy model: $n(\lambda) = A_n + \frac{B_n}{\lambda^2} + \frac{C_n}{\lambda^4}$, where $n$ is the refractive index, $\lambda$ is the wavelength, and A, B, and C were assumed to be 1.55, 0.01, and 0, respectively, as values for transparent organic films. All measurements were performed under ambient conditions.

Attenuated total reflection-Fourier transform infrared (ATR-FTIR) spectra were recorded on a Bruker VERTEX 70 spectrometer equipped with an ATR diamond single reflection accessory. The measurement resolution was 4 $cm^{-1}$ and the spectra were collected in the range of 4000–400 $cm^{-1}$, with 32 scans for each sample. Atmospheric compensation and baseline correction were applied to the collected spectra using OPUS spectroscopy software (v7.0) (Bruker Optics).

Differential scanning calorimetry (DSC) measurements were conducted to measure the thermal transitions of the polymers. The measurements were performed on a TA-Instruments Q1000 DSC by heating–cooling-heating scans with heating–cooling rates of 10 °C $min^{-1}$.

### VPI process development

**VPI process parameters.** About 40 nm thick spin-coated POAcSt, PNMA and P*t*BMA samples on Si(100) were infiltrated with TMA (Strem, ≥98%) in a custom-built ALD reactor. For the VPI experiments, the samples were maintained at 85 °C. The infiltration process was performed as follows: first, the sample was loaded onto the heated substrate holder and the chamber was evacuated to reach a base pressure of $10^{-5}$ mbar. Afterwards the chamber valve to the pump was closed and TMA was pulsed for 10 s, 2 × 20 s or 40 s, respectively. In the case of 2 × 20 s, the chamber was evacuated to the base pressure in-between the two TMA pulses. The pressure within the chamber was constantly rising during the TMA pulse, tracked to a read-out value of 2 mbar, which was reached after the first 5 s. However, a maximum chamber pressure of the TMA vapor pressure of ∼100 mbar would be possible with a reactor wall temperature of 60 °C.[45] Then, the chamber was evacuated again, and a 1 s water pulse was applied to entrap the infiltrated TMA, before removing the sample from the reactor.

**Analysis of the infiltrated samples.** The bare and the infiltrated samples were analyzed by XPS and IR spectroscopy. XPS spectra were recorded using a ThermoFisher K-alpha + XPS Surface Analysis instrument. The instrument uses a monochromatic Al Kα X-ray source (1486.6 eV, 1.2 kV). It is equipped with a monatomic and a gas cluster ion source for etching the sample, a dual beam flood gun for compensating the possible charge effects and with the X-ray source. The XPS depth profiles to determine the composition of the polymers were recorded by using defined etching times of Ar sputtering (500 eV for 30 s or 45 s depending on sample thickness). For the estimation of the element content, the area under the core level spectrum of the Al 2p peak for the aluminum content, the C 1s peak for the carbon content, the O 1s peak for the oxygen content and the Si 2p peak for the silicon content was determined and correlated using the Avantage software. The atomic % of each element was calculated by integrating each individual spectrum after baseline correction.

FT-IR spectra of the thin films were measured using a Nicolet 6700 FT-IR spectrometer with Attenuated Total Reflectance (ATR) crystal attachment: at first, a background of the dry crystal in air is recorded with a resolution of 1.0 $cm^{-1}$ and 100 scans. This background is subtracted from all recorded experimental spectra to cancel out backside refection and eliminate contributions from the tool and the atmosphere. Sampling time is approximatively 6–9 seconds.

### DFT calculations

**Geometry optimization and energy calculation.** The geometry optimization for the pure polymers POAcSt, PNMA, P*t*BMA and their reaction products R1 and R2 with TMA was done by density functional theory (DFT) using the Quickstep module[46] based on the Gaussian and plane waves method (GPW) as implemented in cp2k.[47] The Perdew–Burke–Ernzerhof (PBE) exchange–correlation functional[48,49] with Grimme's dispersion correction D3[50] was used to calculate IR intensities approximately while a 16 Å cutoff was applied. A double-zeta basis set (DZVP-MOLOPT-SR-GTH)[51] was used together with the corresponding Goedecker–Teter–Hutter (GTH) pseudopotentials.[52]

The isolated polymers with two functional groups each in gas phase were modeled with the molecular builder and visualization tool Avogadro[53] and a full geometry optimization and potential energy calculation was carried out.

The calculated potential energies in eV of the products were used to calculate the potential energy differences for the studied reaction paths by subtracting the product energies (from the two pathways R2 and R1) from the educt energies (TMA plus polymer).

**Computational vibrational analysis.** The previously for minimum energy optimized structures were used to do a vibrational analysis, where the IR intensities are calculated as the derivative of the dipole along the normal modes in a static calculation. This is done using DFT with settings similarly as have been used for the geometry optimization. The final IR spectra were computed using the general molecular and electronic structure processing program (Molden),[54,55] estimating the IR spectrum by applying a Lorentzian distribution to the intensities of the normal modes. The resulting frequencies were not adjusted with a multiplication factor as sometimes done to align them with experimental values.[39]

For a deeper look into the specifics and different methods to calculate vibrational spectra from *ab initio* molecular dynamics reading this study from B. Kirchner *et al.*[56] is highly advised.

## Conflicts of interest

There are no conflicts to declare.

## Acknowledgements

The authors would like to thank David de Roest, Yoann Tomczak and Hessel Sprey from ASM Belgium for their support for XPS and FT-IR metrology as well as for the fruitful discussions.

The authors L. M., F. Z., T. D. K. and A. D. are grateful for funding and support from the "Deutsche Forschungsgemeinschaft" (DFG) within the SFB-TR 87

 

Collaborative Research Center. This research received funding from the Netherlands Organization for Scientific Research (NWO, Grant number 731.016.302) in the framework of the Innovation Fund Chemistry. The authors F. Z. and T. D. K. would like to acknowledge the Paderborn Center for Parallel Computing (PC2) for computing time on the FPGA-based supercomputer NOCTUA and the Jülich Supercomputing Centre (JSC) for computing time on the GCS Supercomputer JUWELS.

## References

1 K. Ashurbekova, K. Ashurbekova, G. Botta, O. Yurkevich and M. Knez, *Nanotechnology*, 2020, **31**, 342001.
2 K. J. Yu, Z. Yan, M. Han and J. A. Rogers, *npj Flexible Electron.*, 2017, **1**, 4.
3 K. Gregorczyk and M. Knez, *Prog. Mater. Sci.*, 2016, **75**, 1–37.
4 C. Sanchez, P. Belleville, M. Popall and L. Nicole, *Chem. Soc. Rev.*, 2011, **40**, 696.
5 X. Meng, *J. Mater. Chem. A*, 2017, **5**, 18326–18378.
6 S. M. George, *Chem. Rev.*, 2010, **110**, 111–131.
7 M. Leskelä and M. Ritala, *Thin Solid Films*, 2002, **409**, 138–146.
8 P. Sundberg and M. Karppinen, *Beilstein J. Nanotechnol.*, 2014, **5**, 1104–1136.
9 R. P. Padbury and J. S. Jur, *J. Phys. Chem. C*, 2014, **118**, 18805–18813.
10 J. C. Spagnola, B. Gong, S. A. Arvidson, J. S. Jur, S. A. Khan and G. N. Parsons, *J. Mater. Chem.*, 2010, **20**, 4213.
11 C. Z. Leng and M. D. Losego, *Mater. Horiz.*, 2017, **4**, 747–771.
12 S.-M. Lee, E. Pippel, U. Gosele, C. Dresbach, Y. Qin, C. V. Chandran, T. Brauniger, G. Hause and M. Knez, *Science*, 2009, **324**, 488–492.
13 R. R. Petit, J. Li, B. Van de Voorde, S. Van Vlierberghe, P. F. Smet and C. Detavernier, *ACS Appl. Mater. Interfaces*, 2021, **13**(38), 46151–46163.
14 M. Putkonen, *in Atomic Layer Deposition of Nanostructured Materials*, John Wiley & Sons, Ltd, 2012, pp. 41–59.
15 A. Devi, *Coord. Chem. Rev.*, 2013, **257**, 3332–3384.
16 S. E. Koponen, P. G. Gordon and S. T. Barry, *Polyhedron*, 2016, **108**, 59–66.
17 A. Sinha, D. W. Hess and C. L. Henderson, *J. Vac. Sci. Technol., B: Microelectron. Nanometer Struct.–Process., Meas., Phenom.*, 2007, **25**, 1721.
18 A. R. Berens and H. B. Hopfenberg, *J. Membr. Sci.*, 1982, **10**, 283–303.
19 T. A. Barbari, *J. Polym. Sci., Part B: Polym. Phys.*, 1997, **35**, 1737–1746.
20 P. M. Budd, N. B. McKeown and D. Fritsch, *J. Mater. Chem.*, 2005, **15**, 1977.
21 Y. Sun, R. P. Padbury, H. I. Akyildiz, M. P. Goertz, J. A. Palmer and J. S. Jur, *Chem. Vap. Deposition*, 2013, **19**, 134–141.
22 R. P. Padbury and J. S. Jur, *Langmuir*, 2014, **30**, 9228–9238.
23 L. Lee, K. H. Yoon, J. W. Jung, H. R. Yoon, H. Kim, S. H. Kim, S. Y. Song, K. S. Park and M. M. Sung, *Nano Lett.*, 2018, **18**, 5461–5466.
24 E. K. McGuinness, F. Zhang, Y. Ma, R. P. Lively and M. D. Losego, *Chem. Mater.*, 2019, **31**, 5509–5518.
25 M. Moshonov and G. L. Frey, *Langmuir*, 2015, **31**, 12762–12769.
26 S. Obuchovsky, I. Deckman, M. Moshonov, T. Segal Peretz, G. Ankonina, T. J. Savenije and G. L. Frey, *J. Mater. Chem. C*, 2014, **2**, 8903–8910.
27 S.-M. Lee, E. Pippel, O. Moutanabbir, J.-H. Kim, H.-J. Lee and M. Knez, *ACS Appl. Mater. Interfaces*, 2014, **6**, 16827–16834.
28 K. E. Gregorczyk, D. F. Pickup, M. G. Sanz, I. A. Irakulis, C. Rogero and M. Knez, *Chem. Mater.*, 2015, **27**, 181–188.
29 K. J. Dusoe, X. Ye, K. Kisslinger, A. Stein, S.-W. Lee and C.-Y. Nam, *Nano Lett.*, 2017, **17**, 7416–7423.
30 E. K. McGuinness, C. Z. Leng and M. D. Losego, *ACS Appl. Polym. Mater.*, 2020, **2**, 1335–1344.
31 Y.-C. Tseng, Q. Peng, L. E. Ocola, D. A. Czaplewski, J. W. Elam and S. B. Darling, *J. Mater. Chem.*, 2011, **21**, 11722.
32 Y.-C. Tseng, Q. Peng, L. E. Ocola, D. A. Czaplewski, J. W. Elam and S. B. Darling, *J. Vac. Sci. Technol., B: Nanotechnol. Microelectron.: Mater., Process., Meas., Phenom.*, 2011, **29**, 06FG01.
33 Y.-C. Tseng, Q. Peng, L. E. Ocola, J. W. Elam and S. B. Darling, *J. Phys. Chem. C*, 2011, **115**, 17725–17729.
34 C. A. Wilson, R. K. Grubbs and S. M. George, *Chem. Mater.*, 2005, **17**, 5625–5634.
35 Q. Peng, Y.-C. Tseng, S. B. Darling and J. W. Elam, *Adv. Mater.*, 2010, **22**, 5129–5133.
36 Q. Peng, Y.-C. Tseng, S. B. Darling and J. W. Elam, *ACS Nano*, 2011, **5**, 4600–4606.
37 B. Gong and G. N. Parsons, *J. Mater. Chem.*, 2012, **22**, 15672.
38 M. Biswas, J. A. Libera, S. B. Darling and J. W. Elam, *Chem. Mater.*, 2014, **26**, 6135–6141.
39 E. C. Dandley, C. D. Needham, P. S. Williams, A. H. Brozena, C. J. Oldham and G. N. Parsons, *J. Mater. Chem. C*, 2014, **2**, 9416–9424.
40 S. Bienz, L. Bigler, T. Fox and H. Meier, *Spektroskopische Methoden in der organischen Chemie*, Georg Thieme Verlag, Stuttgart, 9th edn, 2016.
41 D. N. Goldstein, J. A. McCormick and S. M. George, *J. Phys. Chem. C*, 2008, **112**, 19530–19539.
42 B. G. Frederick, G. Apai and T. N. Rhodin, *Phys. Rev. B: Condens. Matter Mater. Phys.*, 1991, **44**, 1880–1890.
43 G. A. Atiya, A. S. Grady, D. K. Russell and T. A. Claxton, *Spectrochim. Acta, Part A*, 1991, **47**, 467–476.
44 J. P. Merrick, D. Moran and L. Radom, *J. Phys. Chem. A*, 2007, **111**, 11683–11700.
45 J. P. McCullough, J. F. Messerly, R. T. Moore and S. S. Todd, *J. Phys. Chem.*, 1963, **67**, 677–679.

46 J. VandeVondele, M. Krack, F. Mohamed, M. Parrinello, T. Chassaing and J. Hutter, *Comput. Phys. Commun.*, 2005, **167**, 103–128.
47 T. D. Kühne, M. Iannuzzi, M. Del Ben, V. V. Rybkin, P. Seewald, F. Stein, T. Laino, R. Z. Khaliullin, O. Schütt, F. Schiffmann, D. Golze, J. Wilhelm, S. Chulkov, M. H. Bani-Hashemian, V. Weber, U. Borštnik, M. Taillefumier, A. S. Jakobovits, A. Lazzaro, H. Pabst, T. Müller, R. Schade, M. Guidon, S. Andermatt, N. Holmberg, G. K. Schenter, A. Hehn, A. Bussy, F. Belleflamme, G. Tabacchi, A. Glöß, M. Lass, I. Bethune, C. J. Mundy, C. Plessl, M. Watkins, J. VandeVondele, M. Krack and J. Hutter, *J. Chem. Phys.*, 2020, **152**, 194103.
48 J. P. Perdew, K. Burke and M. Ernzerhof, *Phys. Rev. Lett.*, 1996, **77**, 3865–3868.
49 J. P. Perdew, K. Burke and M. Ernzerhof, *Phys. Rev. Lett.*, 1997, **78**, 1396–1396.
50 S. Grimme, J. Antony, S. Ehrlich and H. Krieg, *J. Chem. Phys.*, 2010, **132**, 154104.
51 J. VandeVondele and J. Hutter, *J. Chem. Phys.*, 2007, **127**, 114105.
52 S. Goedecker, M. Teter and J. Hutter, *Phys. Rev. B: Condens. Matter Mater. Phys.*, 1996, **54**, 1703–1710.
53 M. D. Hanwell, D. E. Curtis, D. C. Lonie, T. Vandermeersch, E. Zurek and G. R. Hutchison, *J. Cheminf.*, 2012, **4**, 17.
54 G. Schaftenaar and J. H. Noordik, *J. Comput.-Aided Mol. Des.*, 2000, **14**, 123–134.
55 G. Schaftenaar, E. Vlieg and G. Vriend, *J. Comput. Aided Mol. Des.*, 2017, **31**, 789–800.
56 M. Thomas, M. Brehm, R. Fligg, P. Vöhringer and B. Kirchner, *Phys. Chem. Chem. Chem. Phys.*, 2013, **15**, 6608.
57 J. Slaughter, A. J. Peel and A. E. H. Wheatley, *Chem. Eur. J.*, 2017, **23**(1), 167–175.
58 J. Slaughter, S. A. Molyneux, A. J. Peel and A. E. H. Wheatley, *Organometallics*, 2019, **38**(2), 395–408.